RESEARCH ARTICLE | AUGUST 01 2025

Interplay between ion temperature gradient and parallel velocity gradient instabilities in cylindrical geometry: Water-bag vs 5D gyrokinetics

T. Rouyer ; M. Lesur ; E. Gravier ; X. Garbet ; Y. Sarazin ; K. Lim ; G. Lo-Cascio

Phys. Plasmas 32, 082502 (2025)
https://doi.org/10.1063/5.0274782

Physics of Plasmas ARTICLE pubs.aip.org/aip/pop

Interplay between ion temperature gradient and parallel velocity gradient instabilities in cylindrical geometry: Water-bag vs 5D gyrokinetics

Cite as: Phys. Plasmas **32**, 082502 (2025); doi: 10.1063/5.0274782
Submitted: 8 April 2025 · Accepted: 14 July 2025 ·
Published Online: 1 August 2025

View Online Export Citation CrossMark

T. Rouyer,[1,a)] M. Lesur,[1,2] E. Gravier,[1] X. Garbet,[3,4] Y. Sarazin,[3] K. Lim,[4] and G. Lo-Cascio[5]

AFFILIATIONS

[1]Université de Lorraine, CNRS, IJL, F-54000 Nancy, France
[2]Institut Universitaire de France (IUF), Paris, France
[3]CEA, IRFM, F-13108 Saint-Paul-lez-Durance, France
[4]School of Physical and Mathematical Sciences, Nanyang Technological University, 637371 Singapore
[5]Max-Planck-Institut für Plasmaphysik, Boltzmannstrasse 2, D-85748 Garching bei München, Germany

[a)]Author to whom correspondence should be addressed: timothe.rouyer@outlook.fr

ABSTRACT

We investigate the interplay between ion temperature gradient (ITG) and parallel velocity gradient (PVG) instabilities in cylindrical geometry using a Water-bag model and 5D gyrokinetic simulations with a modified version of the GYSELA code. The Water-bag model provides an analytical dispersion relation, which is compared to linear gyrokinetic simulations. Strong agreement is found between predicted and simulated growth rates and real frequencies, validating GYSELA's applicability to cylindrical systems. The comparison also highlights key parametric dependencies on instability thresholds, including the effects of density profiles, temperature gradients, and velocity shear. Notably, weak temperature gradients are found to stabilize PVG modes, whereas strong temperature gradients tend to destabilize them. Additionally, parallel flow shear is shown to enhance ITG-PVG hybrid modes. These properties are likely to impact the turbulent regime.

I. INTRODUCTION

The understanding and control of turbulence-driven transport remain major challenges in magnetically confined plasmas. Key drivers of turbulence are microinstabilities, which arise due to gradients in density, temperature, and velocity. Among them, the ion temperature gradient (ITG) instability and the parallel velocity gradient (PVG) instability are particularly relevant due to their direct impact on turbulent transport. The ITG instability has been widely studied in toroidal configurations, where it is recognized as a major contributor to turbulent heat transport when the ion temperature gradient exceeds a critical threshold.[1,2] This instability has been extensively analyzed using gyrokinetic theory[3] and simulations, providing insights into its nonlinear saturation mechanisms and interaction with zonal flows.[4]

In contrast, the PVG instability, which arises due to a radial shear in the parallel plasma flow, has received comparatively less attention despite its relevance to drift-wave turbulence and shear-flow-induced transport. PVG turbulence has been theoretically predicted in various plasma configurations, including tokamaks, stellarators, and open-field-line systems.[5,6] Parallel shear flows are naturally present in confined plasmas, particularly in the edge and scrape-off layer (SOL) regions, where they result from neoclassical effects, external momentum injection, plasma-wall interaction, or intrinsic plasma rotation.[7–10] Theoretical studies suggest that PVG-driven turbulence can couple with drift waves, leading to enhanced transport or altered turbulence characteristics depending on the system parameters.[11–13]

While experimental observations of PVG in toroidal devices remain limited, linear plasma devices provide an ideal platform for fundamental studies of PVG-driven turbulence due to their well-controlled boundary conditions and simplified magnetic geometry. PVG-driven turbulence has been experimentally observed in various linear devices, including the Q_T-Upgrade machine, the Santander Plasma Linear Machine (SPLM), and the Plasma Assembly for Nonlinear Turbulence Analysis (PANTA), providing compelling evidence of its role in plasma transport and turbulence dynamics.[14–17]

The Sheath, Plasma Edge and Kinetic Turbulence Radiofrequency Experiment (SPEKTRE)[18] is a new linear plasma device currently under construction at Institut Jean Lamour (IJL). One of the main objectives of SPEKTRE is to investigate turbulence-driven transport,[19] including PVG-driven instabilities and their interactions with other turbulence mechanisms. A recent theoretical development has highlighted the role of impurities in modifying PVG-driven turbulence.[20] The ability to inject controlled impurities in SPEKTRE provides an opportunity to study this systematically predicted impurity-modified PVG (i-PVG) instability. Moreover, SPEKTRE will allow for detailed investigations of the transition between drift-wave-dominated and shear-flow-dominated turbulence regimes, complementing the findings from other linear devices.

The interplay between ITG and PVG instabilities remains an open problem, even in cylindrical configurations. Previous studies have suggested that PVG turbulence can either suppress or enhance ITG-driven transport, depending on parameters such as flow shear magnitude, collisionality and temperature gradients.[21–24] The extent to which PVG turbulence interacts with ITG modes, as well as the conditions under which it dominates turbulent transport, requires further investigation. In this study, the linear properties of ITG and PVG instabilities in cylindrical geometry are investigated using two complementary approaches. First, a Water-bag kinetic model is used to derive an analytical dispersion relation for ITG and PVG modes, providing insight into their parametric dependencies and stability thresholds. The Water-bag model has been successfully applied to ITG turbulence and drift-wave instabilities in cylindrical geometry[19,25] but has not yet been used to study PVG instabilities. By extending the Water-bag formalism, this study aims to provide a theoretical framework for analyzing ITG–PVG interactions in cylindrical geometry. Second, full-f 5D gyrokinetic simulations are performed using the GYSELA code,[26] which has been adapted for cylindrical configurations. Originally designed for toroidal gyrokinetic simulations, GYSELA has been modified by removing toroidal curvature terms and adjusting equilibrium profiles to match cylindrical setups. The comparison between Water-bag predictions and gyrokinetic simulations allows for the validation of linear theories, which provide analytical instability thresholds, as well as insight into the role of finite Larmor radius (FLR) effects and flow shear stabilization mechanisms.

A kinetic treatment of the problem has been chosen over a fluid one. Fluid models overestimate the ITG instability growth rate by approximately a factor of 1.5 compared to kinetic models.[19] As we will see in Sec. III D, the kinetic and fluid instability thresholds are also different. Furthermore, in all the simulations we perform, the phase velocity is of the same order of magnitude as the ion thermal velocity ($v_\varphi = \omega/k_\parallel \sim v_{T_i} \sim 10^5\ \mathrm{m\ s^{-1}}$), meaning that the instability growth rate is strongly dependent on resonant wave–particle interactions, which are not described by fluid models.

This paper is organized as follows. Section II presents the numerical model and describes the modifications made to GYSELA for cylindrical simulations. Section III introduces the Water-bag model and derives the dispersion relation for ITG and PVG instabilities. Section IV compares the analytical predictions with gyrokinetic simulations, highlighting agreements and discrepancies. Section V summarizes the findings and discusses future directions, including nonlinear turbulence studies.

II. NUMERICAL MODEL

The gyrokinetic framework allows for time scale separation between the fast gyromotion of charged particles and the slow drift motion across magnetic field lines. A system of coordinates is introduced, describing the evolution of the system in the gyro-center phase-space rather than in the particle phase-space. As a result, low-frequency electrostatic fluctuations can be described at a reduced computing time cost thanks to the elimination of the gyroangle coordinate. The symmetry and energy conservation law of the equations are ensured by using a Hamiltonian representation.[3] The code we describe below is based on this type of model.

A. The GYSELA code

The full-f gyrokinetic code GYSELA[26] enables the study of the interplay between the ITG and PVG instabilities in a 5D phase-space ($\mathbf{x}_{GC,s}$, $v_{G\parallel,s}$, μ_s). These quantities stand for the gyro-center position, the parallel velocity, and the magnetic moment, respectively. The code solves for each ion species the gyrokinetic equation coupled to the quasi-neutrality equation, so the ion distribution function of each ion species $\bar{F}_s$ (the subscript s stands for the species considered) is calculated self-consistently with the electric potential Φ. Considering adiabatic electrons, the model in the version of GYSELA we used reads

$$B^*_{\parallel,s}\frac{\partial \bar{F}_s}{\partial t} + \nabla\cdot\left(B^*_{\parallel,s}\frac{d\mathbf{x}_{GC,s}}{dt}\bar{F}_s\right) + \frac{\partial}{\partial v_{G\parallel,s}}\left(B^*_{\parallel,s}\frac{dv_{G\parallel,s}}{dt}\bar{F}_s\right) = \mathcal{S}(\bar{F}_s), \tag{1}$$

$$en_{e_0}\left(\frac{\Phi - \langle\Phi\rangle_{FS}}{T_{e_0}}\right) - \sum_s Z_s\nabla_\perp\cdot\left(\frac{n_{s_0}}{B_0\Omega_{c,s}}\nabla_\perp\Phi\right) = \sum_s Z_s\int dv_s\mathcal{J}\left[\bar{F}_s - \bar{F}_{eq,s}\right], \tag{2}$$

with

$$\mathbf{B}^*_{\mathbf{s}} = \mathbf{B} + \frac{m_s}{q_s}v_{G\parallel,s}\nabla\times\mathbf{b}. \tag{3}$$

The terms in Eq. (2) are, from left to right, the adiabatic electrons' response, the polarization density in the limit of large wavelengths compared to the Larmor radius, and the particle density fluctuations. $B^*_{\parallel,s}$ is obtained by projecting Eq. (3) on $\mathbf{b} = \mathbf{B}/B$, the unit vector along the magnetic field direction at the guiding-center position, with m_s the mass of the considered species and $q_s = Z_s e$ its charge. An ion species s is also characterized by its density at the initial time n_{s_0} and its cyclotron pulsation $\Omega_{c,s} = q_s B_0/m_s$. The initial electron density n_{e_0} and the initial electron thermal energy T_{e_0}, also appear in the equation system above.

The notation $\langle\ldots\rangle_{FS} = \int\int \ldots J_\chi d\theta d\varphi / \int\int J_\chi d\theta d\varphi$ indicates a flux-surface averaged quantity, J_χ being the Jacobian in space. The gyroaverage operator is applied to the ion distribution function to account for FLR effects and is written as $\mathcal{J}[\ldots] = \oint \ldots d\varphi_c/2\pi$, with φ_c the gyro-phase angle. The operator performs a spatial transformation from particle to gyrocenter coordinates, effectively decoupling the fast gyromotion from the guiding-center dynamics. The bar in $\bar{F}_s \equiv \mathcal{J}[F_s]$ refers to the gyroaverage operation on the ion distribution function. $dv_s = J_{v,s}d\mu dv_\parallel$ is the infinitesimal volume element in the velocity space and depends on $J_{v,s} = 2\pi B^*_{\parallel,s}/m_s$, the Jacobian in velocity space. GYSELA can model both neoclassical and turbulent transport channels self-consistently, taking into account the synergies between them.[27]

All the quantities in GYSELA are normalized to reference values as follows: the mass is normalized to m_0, the number of charges to Z_0, the density to n_0, the thermal energy to T_0, the magnetic field to B_0, the electric potential to T_0/Z_0e, the length scales to a reference Larmor radius $\rho_0 = \sqrt{T_0 m_0}/Z_0 e B_0$, the time scales to the inverse of a reference cyclotron pulsation $\Omega_{c0} = Z_0 e B_0/m_0$, the drift velocities to a reference thermal velocity $v_{T_0} = \sqrt{T_0/m_0}$, and the toroidal velocity of species s to $v_{T_0,s} = v_{T_0}\sqrt{m_0/m_s}$. It should be noted that in GYSELA, for an infinite safety factor, the toroidal velocity and the parallel velocity are analogous. The density and temperature gradients are normalized to R_0 the major radius of the torus at the magnetic axis.

In this paper, the source terms $\mathcal{S}(\bar{F}_s) = S_{heat} + S_{mom}$ include contributions from a pure heat source S_{heat} and from a pure momentum source S_{mom}. The turbulence is forced with S_{heat} in the flux-driven regime of the code, and allows simulations to reach a steady state. We use the momentum source to create a parallel velocity gradient in the radial direction that causes the PVG instability. The source terms are obtained by decomposing the energy-dependent part of the source based on orthogonal Hermite and Laguerre polynomials. Following the method presented in Ref. 28, the two source terms mentioned above take the following form:

$$S_{heat} = \frac{S_0^E S_r^E}{\sqrt{2}\pi^{3/2} T_{sce}^{5/2}} \left[\bar{v}_{G\parallel}^2 - \frac{1}{2} - \frac{J_{\parallel B}}{2 - J_{\parallel B}^2}(2 - \bar{\mu})(2\bar{v}_{G\parallel} - J_{\parallel B}) \right] e^{-\bar{v}_{G\parallel}^2 - \bar{\mu}}, \tag{4}$$

$$S_{mom} = \frac{S_0^{v_\parallel} S_r^{v_\parallel}}{4\pi^{3/2} T_{sce}^2} \left[2\bar{v}_{G\parallel}(2 - \bar{\mu}) - J_{\parallel B}(1 + 2\bar{v}_{G\parallel}^2 - \bar{\mu}) \right] e^{-\bar{v}_{G\parallel}^2 - \bar{\mu}}. \tag{5}$$

In both expressions, the parallel velocity is normalized with $\bar{v}_{G\parallel} = v_{G\parallel}/\sqrt{2T_{sce}/m_s}$, the magnetic moment with $\bar{\mu} = \mu B/T_{sce}$ and the parallel current $J_\parallel$ with $J_{\parallel B} = \sqrt{2T_{sce}} J_\parallel / B^2$, where T_{sce} refers to the source of thermal energy normalized to T_0 and is fixed at 1.5 for the heat source and 1 for the momentum source. S_0^E and $S_0^{v_\parallel}$ are, respectively, the normalized amplitude of the heat source and the momentum source. The source radial profiles, denoted as S_r^E and $S_r^{v_\parallel}$, and represented in Fig. 1, depending on the position of the source ρ_s along the normalized radius $\rho = r/a$, a being the minor radius, and on the width of the source L_s

$$S_r^E = -\frac{1}{2}\left[\tanh\left(\frac{\rho - \rho_s - 3L_s}{L_s} \right) + \tanh\left(\frac{\rho_s - 3L_s - \rho}{L_s} \right) \right], \tag{6}$$

$$S_r^{v_\parallel} = \exp\left(\frac{-(\rho - \rho_s)^2}{10 L_s^2} \right). \tag{7}$$

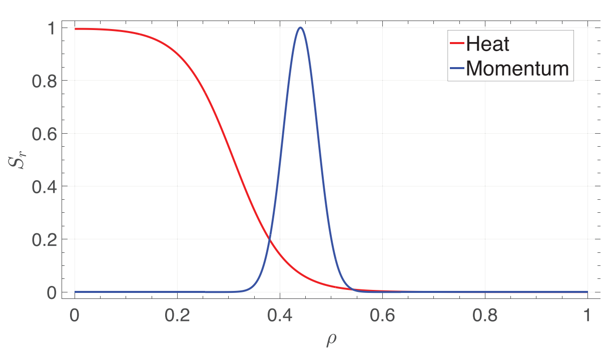

FIG. 1. Radial profiles of heat and momentum sources applied to the ions in GYSELA.

Note that momentum sources resulting from neutral beam injection in tokamak plasmas are likely broader than the one retained in present simulations and depicted in Fig. 1 (cf., e.g., Ref. 29) However, the scope of this paper is the study of PVG and ITG instabilities in the linear regime, rather than taking into account the nonlinear effects linked to the more complex parallel velocity profile of experimental devices.

B. Cylindrical version of GYSELA

To predict the instabilities in linear devices with GYSELA, we select certain input parameters to modify the original geometry of the code from toroidal to a cylindrical one. First, we take a high value for the aspect ratio $1/\epsilon = R_0/a$ so the curvature radius of the torus can be considered infinite. The magnetic drift terms, due to the gradient and the curvature of the magnetic field, are set to zero in the expression of the drift velocity $\mathbf{v}_D$. The plasma current along the magnetic axis is weak in a linear device, meaning that the poloidal component of the magnetic field is negligible. To take this property into account, the safety factor q is set to a very high value. Note that the code in its non-modified version applies periodic boundary conditions to the toroidal direction, meaning that the system is treated as an infinite cylinder in the cylindrical version. With these parameters, the geometry in GYSELA can be approximated to a cylinder locally. We developed an analytical model, described in Sec. III, to verify the ability of GYSELA to correctly estimate linear results in cylindrical machines using this set of parameters.

III. ANALYTICAL LINEAR STUDY

A. The water-bag model

As a means of comparison between GYSELA in the cylindrical approximation and our analytical model, we use the growth rate and the angular frequency of the unstable modes. To obtain said quantities, one must first determine the dispersion relation of the problem. We chose to use a Water-bag[25,30] approach. The idea is to take advantage of Liouville's phase space conservation property. For the collisionless gyrokinetic equation, the distribution function $\bar{F}_s$ is constant along the characteristics

$$\frac{\partial \bar{F}_s}{\partial t} + \mathbf{v}_D \cdot \nabla \bar{F}_s + \dot{v}_\parallel \frac{\partial \bar{F}_s}{\partial v_\parallel} = 0, \tag{8}$$

with $\mathbf{v}_D$ is the drift velocity. This property allows us to perform a discretization of the continuous distribution function into a set of "bags," each bag corresponding to a certain array of values for $v_\parallel$. Let us describe $\bar{F}_s$ with a Heaviside step-function

$$f_{WB}(\mathbf{r}, v_\parallel, t) = \sum_{j=1}^{M} A_j \left[H(v_\parallel - v_j^-(\mathbf{r}, t)) - H(v_\parallel - v_j^+(\mathbf{r}, t)) \right], \tag{9}$$

where M represents the number of bags and H is the Heaviside function. In the case without collision, the bag heights A_j are exact invariants of the problem. This expression of $\bar{F}_s$ can then be injected into the Vlasov equation defined in Eq. (8) to obtain the contour equations

$$\frac{\partial v_j^{\pm}}{\partial t} + \mathbf{v}_D \cdot \nabla v_j^{\pm} = \dot{v}_j^{\pm} = \frac{q_s \bar{E}_{\parallel}}{m_s}. \tag{10}$$

The symbol "+" in the contours $v_j^{\pm}$ indicates a parallel velocity higher than a given value, while the symbol "−" corresponds to parallel velocities lower than this value (see Fig. 2). The quantity $\bar{E}_{\parallel} = -\nabla_{\parallel}(J_0\Phi)$ is the parallel component of the electric field applied to the gyrocenters, with J_0 the zeroth-order Bessel function of argument $k_\perp \rho_{c,s}$ corresponding to the Fourier transform of the gyroaverage operator $\mathcal{J}$. $k_\perp$ is the perpendicular wavenumber and $\rho_{c,s}$ is the Larmor radius of species s. There is a contour equation per value of magnetic moment μ, since this quantity is just a parameter in the gyrokinetic model. In Eq. (10), the time evolution of the distribution function is entirely described by its contours $v_j^{\pm}(\mathbf{r}, t)$, i.e., the distribution of the bags along the $v_{\parallel}$-axis. Doing so eliminates the $v_{\parallel}$ variable from the Vlasov equation, replacing the $\partial_{v_{\parallel}}$ operator by a finite sum on the parallel velocity. The $v_{\parallel}$ dependence of the gyrokinetic equation is retrieved through the contours $v_j^{\pm}$. With this representation of $\bar{F}_s$, one has to handle M fluid equations, one for each bag, instead of a gyrokinetic equation, while still retaining kinetic effects. Indeed, a density $n_j = A_j(v_j^+ - v_j^-)$ and a mean velocity $u_j = (v_j^+ + v_j^-)/2$ can be defined for each bag, denoted with the subscript j. The different fluids are coupled through the quasineutrality equation. The gyrokinetic model is recovered by considering an infinite number of bags. However, as we will see in Sec. IV, a finite number of bags is sufficient to find a good estimation of the kinetic linear growth rates, both for ITG and PVG instabilities. One must note that the Water-bag model is not an approximation of the kinetic equation of motion, but the choice of a particular form for its solutions. Describing the continuous distribution function with Water bags should then be seen as an exact reduction of the phase space dimension.

The Water-bag model can describe any distribution function by choosing appropriate values for A_j and $v_j^{\pm}$. To study the ITG instability, we take a Maxwellian distribution function initially centered at $v_{\parallel} = 0$. The contours at the initial time are then symmetric and take the form $v_j^+ = a_j$ and $v_j^- = -a_j$. To correctly model the PVG instability, however, a parallel velocity $v_{\parallel 0}(r)$ at equilibrium must be considered. The corresponding distribution function is centered on $v_{\parallel 0}$, but its shape remains the same, i.e., a Maxwellian. As a result, the contours at equilibrium are centered around $v_{\parallel 0}$, which can be nonzero, and must now be written as $v_j^+ = a_j^+$ and $v_j^- = -a_j^-$, which is new when compared to Refs. 19, 25, and 30. A distribution function obtained with the Water-bag model is depicted in Fig. 2. Here, we consider a regular distribution of the contours at equilibrium, so the interval $\Delta a = 2a_{max}/(2M-1)$ between each contour is the same. The parameter a_{max} is the contour corresponding to the maximum absolute value of parallel velocity taken into account in the Water-bag model.

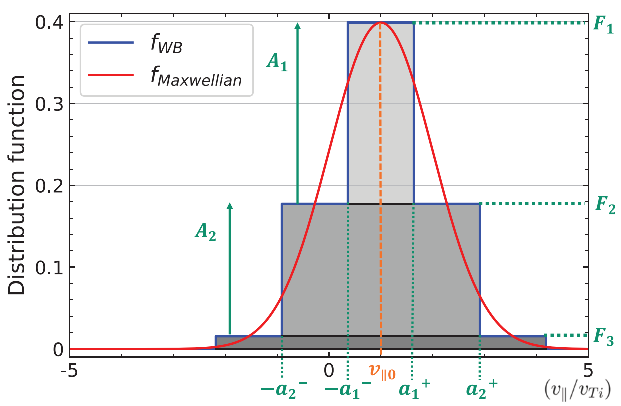

FIG. 2. Continuous distribution function (in red) described by a Water-bag distribution function (in blue) for $M = 3$ plotted against the parallel velocity. $A_j = F_j - F_{j+1}$ is the j^{th} bag height, with F_j the value of the distribution function for this bag. The symbol "+" in the contours $a_j^{\pm}$ indicates a parallel velocity higher than $v_{\parallel 0}$, while the symbol "−" corresponds to parallel velocities lower than $v_{\parallel 0}$.

We consider a plasma with a cylindrical geometry (r, θ, z) immersed in a magnetic field $\mathbf{B} = B\mathbf{u}_z$, with $\mathbf{u}_z$ the unit vector in the axial direction is constant in time and space. Collisions are neglected, so the Water-bag model can be applied to the ion distribution function. Although the introduction of collisions to the model could change the quantitative results of the paper, the trends should remain the same. We assume small wave pulsations ω compared to the cyclotron pulsation $\Omega_{c,s}$, so that plasma fluctuations are slow compared to $\Omega_{c,s}^{-1}$. Since $\mathbf{B}$ is homogeneous and only along the $\mathbf{u}_z$ direction, the magnetic curvature and gradient drifts vanish, and the only guiding-center drift remaining is the electric drift. Thus, the ion guiding-center velocity $\mathbf{v}_D$ is written as follows:

$$\mathbf{v}_D = v_{\parallel}\mathbf{u}_z + \frac{\bar{\mathbf{E}} \times \mathbf{B}}{B^2}, \tag{11}$$

with $\bar{\mathbf{E}} = -\nabla(J_0\Phi)$ the electric field undergone by the guiding centers. For the rest of this paper, we consider a single ion species, whose associated quantities are denoted with the subscript i and electrons denoted with the subscript e. The ion density is obtained via Eq. (10), linked to $v_j^{\pm}$ through the equation coupling the bags

$$n_i = \int \bar{F}_i dv_{\parallel} = \sum_{j=1}^{M} A_j\left[v_j^+ - v_j^-\right], \tag{12}$$

with $\bar{F}_i$ as the continuous distribution function of the ion species considered. We take the phase velocity of the instabilities to be of the same order as the ion thermal speed, meaning that the electron inertia can be neglected. In other words, an adiabatic response is assumed for the electrons. The perturbing potential energy is also taken to be small compared to the electron thermal energy. These hypotheses give a relation between the perturbed electron density amplitude n_{e_1} and the perturbed electric potential amplitude ϕ

$$n_{e_1} = \frac{e\phi}{T_{e_0}} n_{e_0}. \tag{13}$$

The initial electric potential is taken to be zero. The ion and electron populations are coupled through the quasineutrality equation, which reads

$$n_e = Z_i\left[\int \mathcal{J}[\bar{F}_i]dv_{\parallel} + \nabla_\perp \cdot \left(\frac{n_{i_0}}{\Omega_{c,i}B}\nabla_\perp\Phi\right)\right]. \tag{14}$$

The second term on the right-hand side is the polarization density, due to the polarization drift. It accounts for the time evolution of the electric field, which modifies the Larmor radius of the electric particles during a cyclotron period. This phenomenon gives rise to a drift perpendicular to the magnetic field. The drift causes a current, whose divergence leads to a charge accumulation, i.e., the polarization density. This term replaces the displacement current in the quasineutral limit of gyrokinetic equations. This operation improves the stability of the numerical scheme.

B. Dispersion relation for the water-bag model

We consider small perturbations around the equilibrium, allowing us to separate the velocities $v_j^\pm$, the electric potential Φ, and the densities n_i and n_e, into an equilibrium term (designated by the subscript "0") and a linear perturbation term (designated by the subscript "1"). The perturbations are decomposed into a Fourier basis in the θ and z directions. The aforementioned quantities read as follows:

$$v_j^\pm = a_j^\pm(r) + w_j^\pm(r)\,\exp\left[i(m\theta + k_\parallel z - \omega t)\right] + c.c., \tag{15}$$

$$\Phi(r,\theta,z,t) = \phi(r)\,\exp\left[i(m\theta + k_\parallel z - \omega t)\right] + c.c., \tag{16}$$

$$n_i = n_{i_0}(r) + n_{i_1}(r)\,\exp\left[i(m\theta + k_\parallel z - \omega t)\right] + c.c., \tag{17}$$

$$n_e = n_{e_0}(r) + n_{e_1}(r)\,\exp\left[i(m\theta + k_\parallel z - \omega t)\right] + c.c., \tag{18}$$

with m is linked to the azimuthal wavenumber through $k_\theta = m/r$, $k_\parallel$ the parallel wavenumber, and ω the wave angular pulsation. As we mentioned before, there is no electric potential ϕ_0 at equilibrium. The quasineutrality at $t = 0$ yields $Z_i n_{i_0} = n_{e_0}$. The equilibrium and linear terms of Eq. (12) give, respectively,

$$n_{i_0} = \sum_{j=1}^{M} A_j\left[a_j^+ + a_j^-\right], \tag{19}$$

and

$$n_{i_1} = \sum_{j=1}^{M} A_j\left[w_j^+ - w_j^-\right]. \tag{20}$$

The perturbed velocities $w_j^\pm$ are obtained by injecting Eq. (15) into Eq. (10) and keeping only the first-order terms. Equation (20) then becomes

$$n_{i_1} = J_0\phi\sum_{j=1}^{M} A_j\left[\frac{\frac{q_i}{m_i}k_\parallel^2(a_j^+ + a_j^-) + \frac{k_\theta}{B}k_\parallel\left(a_j^+\frac{da_j^-}{dr} - a_j^-\frac{da_j^+}{dr}\right) - \frac{k_\theta}{B}\omega\left(\frac{da_j^+}{dr} + \frac{da_j^-}{dr}\right)}{(\omega - k_\parallel a_j^+)(\omega + k_\parallel a_j^-)}\right]. \tag{21}$$

Finally, the linearization of the quasineutrality equation defined in Eq. (14) leads to a differential equation for $\phi(r)$

$$\frac{d^2\phi}{dr^2} + \left(\kappa_n + \frac{1}{r}\right)\frac{d\phi}{dr} + \left(Q(r) - k_\theta^2\right)\phi(r) = 0, \tag{22}$$

with $\kappa_n = 1/L_n = \partial_r \ln(n_{i_0})$ is the density gradient length and

$$Q(r) = \frac{1}{r_{L_i}^2}\left[J_0^2\sum_{j=1}^{M}\alpha_j\frac{\left(k_\parallel^2 v_{T_i}^2 - \omega\Omega_j^* - k_\theta k_\parallel r_{L_i}^2\Omega_{c,i}\chi_j\right)}{(\omega - k_\parallel a_j^+)(\omega + k_\parallel a_j^-)} - \frac{\tau}{Z_i}\right]. \tag{23}$$

We define $r_{L_i} = v_{T_i}/\Omega_{c,i}$, $v_{T_i} = \sqrt{T_{i_0}/m_i}$ and $\tau = T_{i_0}/T_{e_0}$. The contours at equilibrium are related through $a_j^- = a_j^+ - 2v_{\parallel 0}$ (see Fig. 2). We have introduced the relative density α_j and the diamagnetic frequency Ω_j^* of the j^{th} bag at the initial time

$$\alpha_j = \frac{n_{0j}}{\sum_{j=1}^{M} n_{0j}} = \frac{2A_j(a_j^+ - v_{\parallel 0})}{n_{i_0}}, \tag{24}$$

$$\Omega_j^* = \frac{k_\theta v_{T_i}^2}{\Omega_{c,i}}\kappa_j, \tag{25}$$

where n_{0j} is the initial density of the j^{th} bag. The radial dependence of the bags appears through the parameters $\kappa_j = \partial_r \ln(n_{0j})$. We also define

$$\chi_j = \frac{\left(a_j^-\frac{da_j^+}{dr} - a_j^+\frac{da_j^-}{dr}\right)}{a_j^+ + a_j^-} = \frac{dv_{\parallel 0}}{dr} - v_{\parallel 0}\kappa_j. \tag{26}$$

Furthermore, we make the hypothesis that the radial dependence of the bags is completely retrieved through the density and temperature gradients, so we can write κ_j as a linear combination of these two gradients

$$\kappa_j = \frac{\left(\frac{da_j^+}{dr} + \frac{da_j^-}{dr}\right)}{a_j^+ + a_j^-} = \frac{1}{2}\left(1 - \frac{\gamma_j}{\alpha_j}\right)\kappa_T + \frac{\gamma_j}{\alpha_j}\kappa_n, \tag{27}$$

with $\kappa_T = 1/L_T = \partial_r \ln(T_{i_0})$ is the temperature gradient length and $\gamma_j = \Delta a(F_j + F_{j+1})/n_{i_0}$.

The quantity $Q(r)$ in Eq. (22) accounts for the linear response of the ion gyrocenter density to the perturbed potential. Compared to other papers treating the subject of ITG and DW instabilities with the Water-bag model,[19,25,30,31] considering an injection of parallel velocity $v_{\parallel 0}$ in the system at equilibrium modifies the differential equation for $\phi(r)$ by introducing a term proportional to χ_j and changing the denominator in Eq. (23). The variable χ_j is of first importance because it contains the PVG instability drive $dv_{\parallel 0}/dr$ and allows us to include the latter in the model. In other words, setting $v_{\parallel 0}$ and $dv_{\parallel 0}/dr$ to zero allows one to retrieve the expression of $Q(r)$ for the ITG instability, like the one derived in Ref. 25. In the same way, the ITG instability drive is entirely contained in κ_j, via κ_T. Setting the latter to zero gives the expression of $Q(r)$ for the pure PVG instability. In the present case, since the DW instability is outside the scope of this article, the electron-neutral collision rate is chosen to be zero and the adiabatic hypothesis for the electrons imposes that their velocity along the axis of the cylinder is also zero.

In an attempt to obtain a dispersion relation analytically while still retaining the radial extent of the perturbation modes, let us constrain the solution to the form $\phi(r) = \phi_0 \exp[g(r)]$ for the potential amplitude, $g(r)$ being a function of its radial profile and ϕ_0 its maximal value on this profile, and inject it in Eq. (22). Then, we can define

$$\kappa_r(r) = -\left[\frac{\partial^2 g}{\partial r^2} + \left(\frac{\partial g}{\partial r}\right)^2 + \left(\kappa_n + \frac{1}{r}\right)\frac{\partial g}{\partial r}\right]. \tag{28}$$

The form of $g(r)$ can be chosen so as to have a simple expression for $\phi(r)$ and enables an easier derivation of the dispersion relation compared to the general case, where the form of the profile of $\phi(r)$ is unspecified. So, this "semi-global" method allows one to partially take into account the radial profile of the perturbation modes.

Finally, the Water-bag model gives a dispersion relation in the form of a $2M^{th}$ order polynomial

$$1 + \frac{Z_i}{\tau} r_{L_i}^2(\kappa_r + k_\theta^2) - \frac{Z_i}{\tau} J_0^2 \left[\sum_{j=1}^{M} \alpha_j \frac{\left(k_\parallel^2 v_{T_i}^2 - \omega\Omega_j^* - k_\theta k_\parallel r_{L_i}^2 \Omega_{c,i}\chi_j\right)}{(\omega - k_\parallel a_j^+)(\omega + k_\parallel a_j^-)}\right] = 0 = \varepsilon(\omega). \tag{29}$$

If we take symmetrical contours for the initial distribution function ($a_j^+ = a_j^- = a_j$) in Eq. (29) and neglect FLR effects, we retrieve the dispersion relation for the ITG modes derived in Ref. 25. Note that a local analysis implies ϕ to be independent of r. In this case, we get the same expression as Eq. (29) but with $\kappa_r = 0$. The global effects in our description are entirely contained in the correction κ_r. In the case where one would want to solve Eq. (22) without restricting $\phi(r)$ to a given form, either a shooting method[32] or a spectral method[33] can be used. However, as we will see in Sec. IV, the "semi-global" dispersion relation defined in Eq. (29) is adequate enough to predict the linear results of the global code GYSELA.

C. Dispersion relation for the fluid model

From Eq. (8), we can also derive the first three fluid moments in cylindrical geometry for ions, respectively, the continuity equation, the momentum conservation equation, and the energy conservation equation

$$\frac{Dn_i}{Dt} + n_i\frac{\partial u_\parallel}{\partial z} - \frac{1}{rB}\frac{\partial\Phi}{\partial\theta}\frac{\partial n_i}{\partial r} + \frac{1}{rB}\frac{\partial\Phi}{\partial r}\frac{\partial n_i}{\partial\theta} = 0, \tag{30}$$

$$m_i n_i\left[\frac{Du_\parallel}{Dt} + \frac{1}{rB}\left(\frac{\partial\Phi}{\partial r}\frac{\partial u_\parallel}{\partial\theta} - \frac{\partial\Phi}{\partial\theta}\frac{\partial u_\parallel}{\partial r}\right)\right] = -\frac{\partial P_\parallel}{\partial z} - n_i q_i\frac{\partial\Phi}{\partial z}, \tag{31}$$

$$\frac{DP_\parallel}{Dt} + 3P_\parallel\frac{\partial u_\parallel}{\partial z} + 2\frac{\partial q_{heat}}{\partial z} + \frac{1}{rB}\left(\frac{\partial\Phi}{\partial r}\frac{\partial P_\parallel}{\partial\theta} - \frac{\partial\Phi}{\partial\theta}\frac{\partial P_\parallel}{\partial r}\right) = 0, \tag{32}$$

where $\frac{D}{Dt} = \frac{\partial}{\partial t} + u_\parallel\frac{\partial}{\partial z}$, $u_\parallel$ is the fluid velocity along z, $P_\parallel$ is the parallel pressure, and q_{heat} is the heat flux. We assume a Maxwellian distribution function, so the latter is zero. Compared to the fluid moments for only ITG, terms with $u_\parallel \neq 0$ appear in all three equations. We linearize Eqs. (30)–(32) and combine them with Eqs. (13) and (14). To simplify, the gyroaverage operator is set to 1, and the polarization term is set to 0 in the quasineutrality equation. We then get the fluid dispersion relation for ITG and PVG

$$\tilde{\omega}^3 + Z_i k_\theta \frac{c_e^2}{\Omega_{c,i}}\kappa_n\tilde{\omega}^2 + \left[Z_i k_\theta k_\parallel \frac{c_e^2}{\Omega_{c,i}}\frac{du_{\parallel 0}}{dr} - k_\parallel^2 c_s^2\right]\tilde{\omega} + Z_i k_\theta k_\parallel^2 \tau \frac{c_e^4}{\Omega_{c,i}}(\kappa_T - 2\kappa_n) = 0, \tag{33}$$

with $\tilde{\omega} = \omega - k_\parallel u_{\parallel 0}$, $c_e = \sqrt{T_{e_0}/m_i}$, and $c_s = \sqrt{(3T_{i_0} + Z_i T_{e_0})/m_i}$ is the ion sound velocity. The subscript "0" refers to the equilibrium term of the fluid quantities. The electric potential at the initial time ϕ_0 is set to zero. The ion pressure and thermal energy are related through $P_{i_0} = n_{i_0} T_{i_0}$.

In the cold ion limit, where we take $T_{i_0} = 0$ and assume a zero Doppler shift ($u_{\parallel 0} = 0$), Eq. (33) is simplified to a second-order polynomial

$$\omega^2 + Z_i k_\theta \frac{c_e^2}{\Omega_{c,i}}\kappa_n\omega + Z_i k_\theta k_\parallel \frac{c_e^2}{\Omega_{c,i}}\frac{du_{\parallel 0}}{dr} - Z_i k_\parallel^2 c_e^2 = 0, \tag{34}$$

which allows us to recover an instability criterion similar to the one found in Ref. 34, showing that the PVG instability is stabilized by the density gradient and is harder to destabilize for short parallel wavelength and long azimuthal wavelength

$$\begin{cases} \dfrac{1}{\Omega_{c,i}}\dfrac{du_{\parallel 0}}{dr} > \dfrac{Z_i}{4}\dfrac{k_\theta}{k_\parallel}\left(\dfrac{c_e}{\Omega_{c,i}}\kappa_n\right)^2 + \dfrac{k_\parallel}{k_\theta} & \text{if } \dfrac{k_\parallel}{k_\theta} > 0 \\ \dfrac{1}{\Omega_{c,i}}\dfrac{du_{\parallel 0}}{dr} < \dfrac{Z_i}{4}\dfrac{k_\theta}{k_\parallel}\left(\dfrac{c_e}{\Omega_{c,i}}\kappa_n\right)^2 + \dfrac{k_\parallel}{k_\theta} & \text{if } \dfrac{k_\parallel}{k_\theta} < 0. \end{cases} \tag{35}$$

D. Linear study of the coexistence of ITG and PVG

We perform a linear study on the coexistence of the ITG and PVG instabilities, with a custom code in cylindrical geometry based on the Water-bag model. It solves Eq. (29) normalized to the reference quantities presented in Sec. II A to determine the growth rate γ and angular frequency ω_r of any given perturbation mode. We run this code to evaluate the influence of κ_T and $dv_\parallel/dr$ on these two quantities. For each point (κ_T, $dv_\parallel/dr$), the code performs a scan in azimuthal mode numbers $m \in [0, 500]$ and axial mode numbers $n \in [0, -75]$. We eliminate the contributions of global effects and gyroaverage on γ and ω_r by choosing $\kappa_r = 0$ and $J_0 = 1$. The quantities are calculated at $\rho = 0.5$. We take $M = 25$ bags to ensure the results are converged. The results are depicted in Fig. 3 for an arbitrary set of normalized parameters. For each point in Fig. 3(a), the corresponding angular frequency ω_r is given in Fig. 3(b), for the same parameters. The same method is applied in Fig. 4, but instead of looking for the most unstable mode, we focus on a specific mode, namely, the mode ($m = 80$, $n = -20$), and neglect the polarization effects. The sign of ω_r depends on the direction of propagation of the perturbation wave compared to the direction of the electron diamagnetic velocity $\mathbf{v}_{\wedge,e} = -\frac{T_e}{eB}(\kappa_{T,e} + \kappa_{n,e})\mathbf{u}_\theta$, with $\mathbf{u}_\theta$ the unit vector in the azimuthal direction. When $\gamma = 0$, the corresponding value of ω_r is not plotted.

Let us focus on the $\eta \geq 0$ domain first, with $\eta = \kappa_T/\kappa_n = L_n/L_T$ the ratio of the ion temperature to ion density gradient

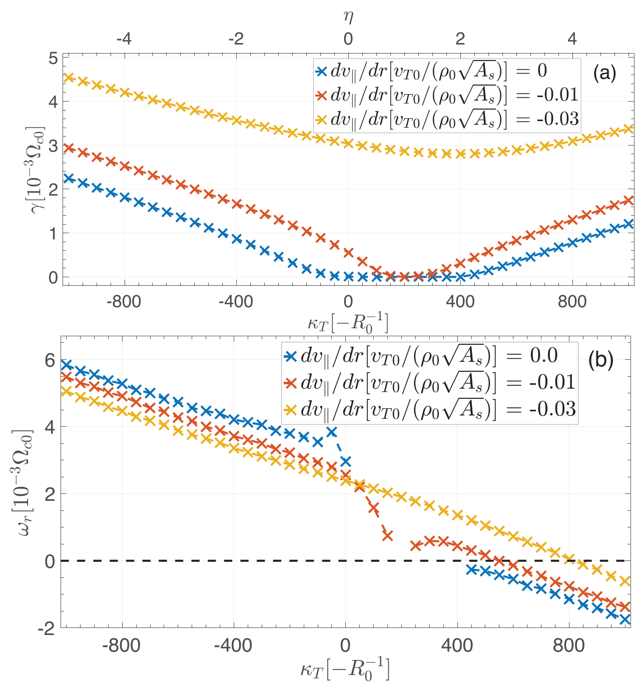

FIG. 3. (a) Instability growth rate γ and (b) angular frequency ω_r for the fastest growing mode, plotted against $\kappa_T[-R_0^{-1}] = -R_0/L_T$, or equivalently $\eta = \kappa_T/\kappa_n$ as indicated at the top, for several values of parallel velocity gradient $dv_\parallel/dr$. Results obtained with a linear cylindrical code based on the Water-bag model and for the arbitrary set of normalized parameters $\kappa_n[-R_0^{-1}] = 200$, $T_i[T_0] = 1$ and $v_{\parallel 0}[v_{T_0}\sqrt{m_0/m_s}] = 0.01$. Values of ω_r corresponding to $\gamma = 0$ are not plotted. The dashed black line indicates $\omega_r = 0$. κ_T and η axes are shared between the two graphs.

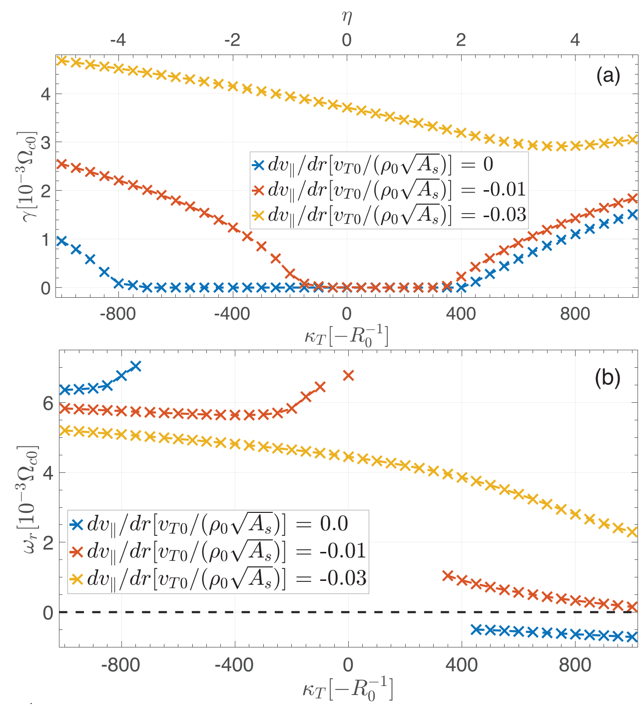

FIG. 4. (a) Instability growth rate γ and (b) angular frequency ω_r for a given perturbation mode (80, -20) with no polarization effects, plotted against $\kappa_T[-R_0^{-1}] = -R_0/L_T$, or equivalently $\eta = \kappa_T/\kappa_n$ as indicated at the top, for several values of parallel velocity gradient $dv_\parallel/dr$. Results obtained with a linear cylindrical code based on the Water-bag model and for the arbitrary set of normalized parameters $\kappa_n[-R_0^{-1}] = 200$, $T_i[T_0] = 1$ and $v_{\parallel 0}[v_{T_0}\sqrt{m_0/m_s}] = 0.01$. Values of ω_r corresponding to $\gamma = 0$ are not plotted. The dashed black line indicates $\omega_r = 0$. κ_T and η axes are shared between the two graphs.

lengths, the latter being set to $\kappa_n = 200$ for this example. By looking at the curve for $dv_\parallel/dr = 0$ in Fig. 3(a), one can note that the growth rate becomes positive only for $\eta > 2$. This result makes sense since the PVG instability needs a parallel velocity gradient to be triggered and the ITG instability appears only when a critical value of η is exceeded.[4] This is consistent with a pure ITG instability in this zero-shear case. This idea is reinforced by the fact that ω_r in Fig. 3(b) for the curve $dv_\parallel/dr = 0$ is negative for $\eta > 2$. For the red curve ($dv_\parallel/dr = -0.01$), a shearing is introduced. Compared to the previous case, γ can now be non-zero in the domain $0 \leq \eta \leq 2$. One can also notice that $\omega_r > 0$ in this range of values, which indicates that the instability, although possibly hybrid between ITG and PVG, is in some sense closer to a PVG. However, this γ_{PVG} is not monotonic. It first decreases before reaching zero, and then its values start increasing. One can make the hypothesis that this initial decrease is due to the stabilizing effect of κ_T on γ_{PVG}, which is consistent with the results found in Ref. 21. If the temperature gradient keeps increasing, the ITG instability eventually becomes dominant [$\omega_r < 0$ in Fig. 3(b)]. In this region, the $dv_\parallel/dr = -0.01$ curve is above the $dv_\parallel/dr = 0$ curve for any given value of η. The reason could be the phenomenon described in Ref. 35, namely, that $dv_\parallel/dr$ strengthens the ITG modes' growth rate, or because ITG and PVG reinforce each other. Finally, if we take a stronger parallel velocity gradient ($dv_\parallel/dr = -0.03$), the stabilizing effect of κ_T on γ_{PVG} is still observed, but is not large enough to compensate for the strong PVG drive, which means that γ is above zero for any value of η. For this large parallel velocity gradient, ω_r stays positive for higher values of η, compared to the case where $dv_\parallel/dr = -0.01$.

Now taking into account negative values of η, we notice an asymmetry in growth rates between positive and negative values of η. In an attempt to explain this, we compare Fig. 4 to the instability threshold in terms of κ_n and κ_T of the mode (80, -20). The results are plotted in Fig. 5 for $dv_\parallel/dr = 0$ and in Fig. 6 for $dv_\parallel/dr = -0.01$. The fluid threshold is obtained by analytically solving Eq. (33). For the kinetic threshold, we solve the following system satisfied by the dielectric plasma function $\varepsilon(\omega)$ [see Eq. (29)], with $J_0 = 1$ and no polarization

$$\varepsilon(\omega) = 0, \tag{36}$$

$$\frac{d\varepsilon}{d\omega}(\omega) = 0.$$

Then, a numerical parametric resolution in terms of ω is done on Eq. (36) for $M = 25$. In Fig. 5, we recover the ITG instability threshold since $dv_\parallel/dr = 0$. There is a stability region around $\kappa_T = 0$ for any value of κ_n. This stability region disappears in Fig. 6, which means that for $dv_\parallel/dr = -0.01$ and κ_n small enough, the plasma is unstable for any values of κ_T because of the destabilization of PVG by the parallel

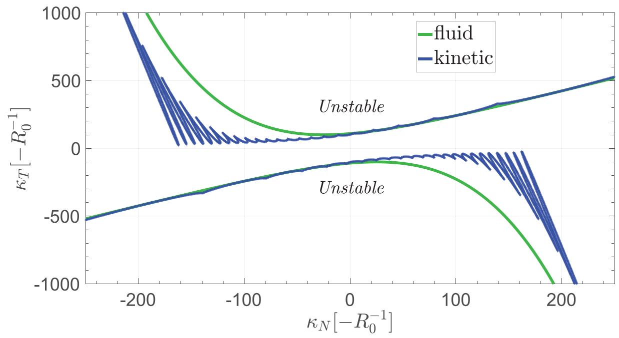

FIG. 5. Instability threshold for the perturbation mode ($m = 80$, $n = -20$). The polarization effects are neglected. We take $T_i[T_0] = 1$, $v_{\parallel 0}[v_{T_0}\sqrt{m_0/m_s}] = 0.01$ and $dv_\parallel/dr[v_{T0}/(\rho_0\sqrt{A_s})] = 0$, with A_s the mass number of the considered species. The kinetic curve is obtained for $M = 25$. The strong fluctuations on the kinetic curve are due to the fact that the instability thresholds in the Water-bag model have a lobe-like structure. This is a consequence of the discretization of the velocity distribution function in this model.

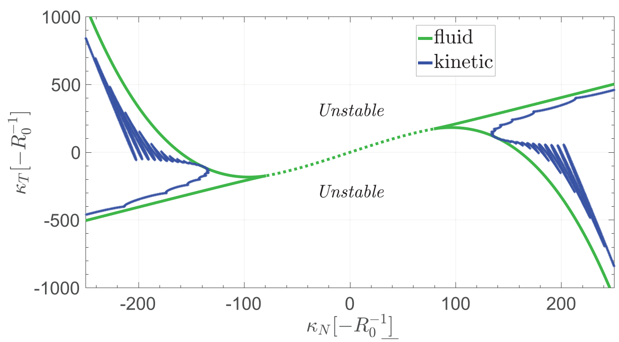

FIG. 6. Same legend as Fig. 5 with $dv_\parallel/dr[v_{T0}/(\rho_0\sqrt{A_s})] = -0.01$. The dashed green line indicates that the two solutions of $\kappa_T[-R_0^{-1}] = f(\kappa_n[-R_0^{-1}])$ are the same for these values of $\kappa_n[-R_0^{-1}]$.

velocity gradient. The comparison of Figs. 5 and 6 with, respectively, the $dv_\parallel/dr = 0$ curve and the $dv_\parallel/dr = -0.01$ curve of Fig. 4(a) allows us to interpret the asymmetry in growth rates in the latter. Indeed, we notice that the values of κ_T for which the growth rate is non-zero in Fig. 4(a) correspond to unstable regions in Figs. 5 and 6. The graphs show that, for a given value of κ_n, reaching an unstable region does not require the same value of κ_T depending on its sign. This asymmetry becomes stronger when the value of κ_n increases. We can also see that for some values of κ_n, the fluid and kinetic thresholds have opposite asymmetries. Nonetheless, they give the same trend when κ_n is high enough, namely, that the plasma is more easily destabilized by the ITG-PVG instability when η is positive.

The evolution of the azimuthal mode number m and the axial mode number n for the fastest growing mode as a function of η is plotted in Fig. 7 for several values of parallel velocity gradient. From these graphs, as well as Fig. 3(b), we can infer that the further ω_r is from zero, the closer the associated m is to zero and the further n is. We also see that the outliers in Fig. 7 can be found in Fig. 3(b) as well. Figures 7(a) and 7(c) show a smooth evolution of (m, n) with η, meaning that there is no jump from an instability branch to another. The evolution

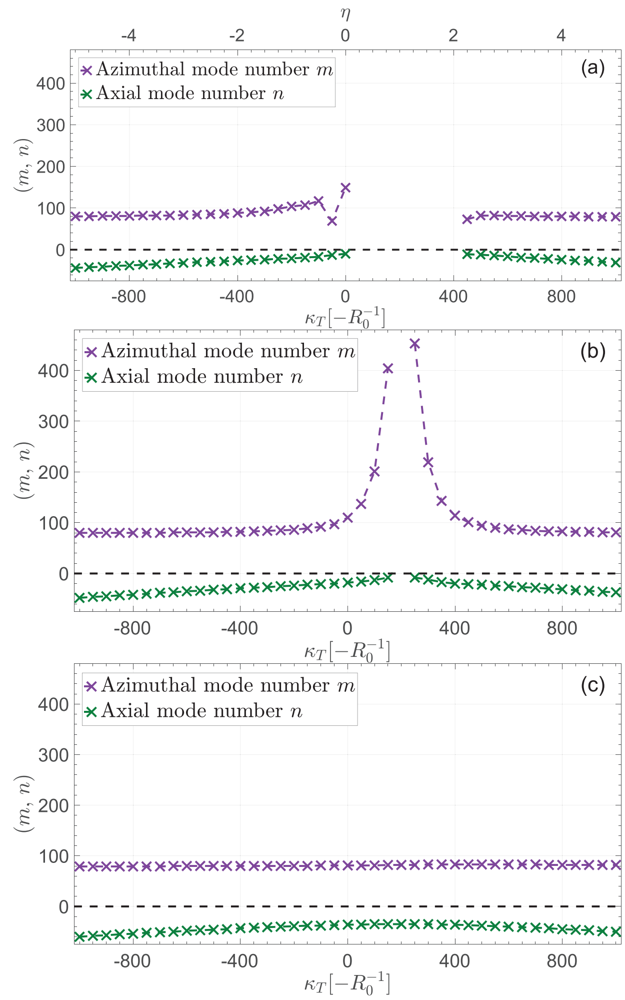

FIG. 7. Azimuthal mode number m and axial mode number n for the fastest growing mode, plotted against $\kappa_T[-R_0^{-1}] = -R_0/L_T$, or equivalently $\eta = \kappa_T/\kappa_n$ as indicated at the top, for (a) $dv_\parallel/dr = 0$, (b)$dv_\parallel/dr = -0.01$, and (c) $dv_\parallel/dr = -0.03$. Results obtained with a linear cylindrical code based on the Water-bag model and for the arbitrary set of normalized parameters $\kappa_n[-R_0^{-1}] = 200$, $T_i[T_0] = 1$ and $v_{\parallel 0}[v_{T_0}\sqrt{m_0/m_s}] = 0.01$. Values of (m, n) corresponding to $\gamma = 0$ are not plotted. The dashed black line indicates $m = 0$ and $n = 0$. κ_T and η axes are shared between the three graphs.

of m is steeper in the region $0 \leq \eta \leq 2$ of Fig. 7(b) compared to Fig. 7(c), but the growth rate is small in this region.

It is also instructive to plot the evolution γ and ω_r of the most unstable mode relative to the parallel velocity gradient for given values of η. These graphs can be found in Fig. 8 for $\kappa_n = 200$. The $\eta = 0$ and $\eta = 1$ curves correspond to pure PVG modes since the ITG instability criterion is not satisfied in these cases. Moreover, in Fig. 8(b), ω_r is positive for these modes, even for small values of parallel velocity gradient. Nonetheless, we see in Fig. 8(a) that $\gamma(\eta = 0)$ is greater than $\gamma(\eta = 1)$, for any value of $dv_\parallel/dr$, once again showing a stabilizing effect of κ_T on γ_{PVG}. The $\eta = 3$ curve corresponds to a situation where both ITG and PVG instability criteria can be satisfied. According to Fig. 8(b), the instability is closer to an ITG for $dv_\parallel/dr > -0.0125$ and

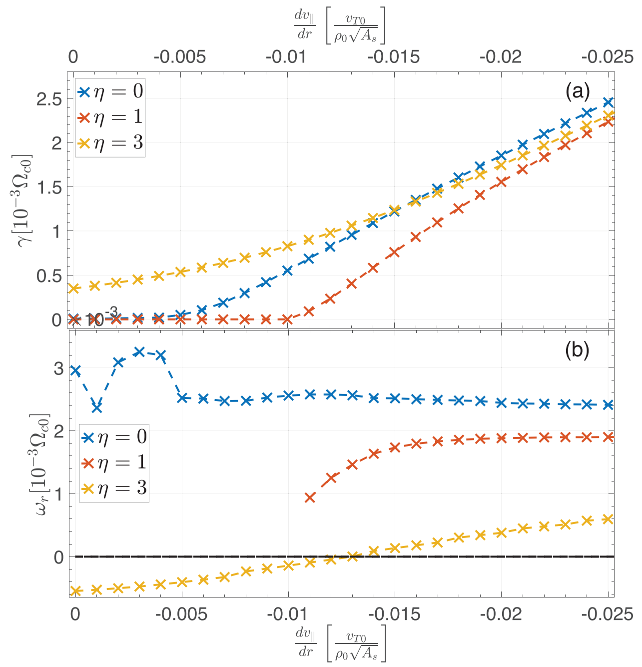

FIG. 8. (a) Instability growth rate γ and (b) angular frequency ω_r for the fastest growing mode, plotted against the parallel velocity gradient $dv_\parallel/dr$, for several values of $\eta = \kappa_T/\kappa_n$. Results obtained with a linear cylindrical code based on the Water-bag model and for the arbitrary set of normalized parameters $\kappa_n[-R_0^{-1}] = 200$, $T_i[T_0] = 1$ and $v_{\parallel 0}[v_{T_0}\sqrt{m_0/m_s}] = 0.01$. Values of ω_r corresponding to $\gamma = 0$ are not plotted. The dashed black line indicates $\omega_r = 0$. $dv_\parallel/dr$ axis is shared between the two graphs.

to a PVG for $dv_\parallel/dr < -0.0125$. For relatively small values of parallel velocity gradient, $\gamma(\eta = 3)$ is above the two other curves. However, when $dv_\parallel/dr$ increases, its evolution is less steep than the $\gamma(\eta = 0)$ and $\gamma(\eta = 1)$ curves. Again, this phenomenon could be explained by the stabilization effect of the ion temperature gradient on the PVG instability or by a competition between ITG and PVG instabilities.

A summary of the results presented in this section can be found in Table I.

IV. COMPARISON BETWEEN GYSELA AND THE ANALYTICAL MODEL RESULTS

The focus of this section is to show that the GYSELA code can predict with good accuracy linear results in devices with cylindrical geometry. We emulate these cylindrical conditions with the parameters defined in Sec. II B. The goal is to calculate the growth rate γ and the angular frequency ω_r of some perturbation modes, with GYSELA on one hand and with the code using Water-bags introduced in Sec. III D on the other hand, and compare them. We perform three types of simulations: one where only the ITG instability is triggered (Sec. IV A), another one where the perturbation modes are only subject to the PVG instability (Sec. IV B), and one where both instabilities are triggered (Sec. IV C). The parameters used in these simulations are summarized in Table II, and the normalization introduced in Sec. II A is applied to all these parameters.

In all the GYSELA simulations, we take deuterium, characterized by its number of charge $Z_i = 1$ and its mass number $A_i = 2$, as the only ion species. The radial domain goes from $\rho_{min} = 0.002$ to $\rho_{max} = 1$. A diffusive buffer is present at the edge to attenuate numerical oscillations. Dirichlet boundary conditions impose that $\phi(\rho_{max}) = 0$, while $E_r = 0$ at $\rho = \rho_{min}$. The problem is solved for $\rho > 0$ to avoid the singularity in $1/r$. Although the point $\rho = 0$ is not contained in the simulation domain, B_0 is calculated on the magnetic axis. All non-axisymmetric fluctuations are forced to zero at both radial boundaries. The parallel velocity is in the range $-7 < v_{\parallel,i} < 7$. For simplicity's sake, the magnetic moment μ is set to zero, meaning that $J_0 = 1$, but FLR effects are still partially taken into account with the polarization term in Eq. (14). The aspect ratio $1/\epsilon$ is set to a high value in an attempt to get close to a cylindrical geometry. In addition, we take a very large value to the safety factor, which allows the toroidal magnetic field component to be overwhelmingly large compared to the poloidal component, rendering the latter negligible. The initial temperature and density radial profiles are described by the same function as the one given in Ref. 26. There are no collisions in the simulations we carried out, so Liouville's phase space conservation property is respected. There is no momentum injection in the "ITG only" simulation, while in the two other ones, $S_0^{v_\parallel}$ is non-zero during a certain time interval (see Table II) to trigger the PVG instability. The heat source is the same in all cases. The growth rates and angular frequencies are all calculated at a certain radius $r = r_p$. The former is computed by performing a linear fit on the linear growth phase of the $\phi(t)$ curve corresponding to the (m, n) mode considered, and the latter by analyzing $|Re(\phi_{m,n})|/|\phi_{m,n}|$ during that phase, $\phi_{m,n}$ being the electric potential in the Fourier space for a given mode and $Re(\phi_{m,n})$ being its real part.

We use the same parameters in the Water-bag model and in the GYSELA simulations described in Table II to determine the growth rates and angular frequencies of several azimuthal mode numbers m for a given axial mode number n. As in Sec. III D, we take $M = 25$ and $J_0 = 1$. However, we refer to Eq. (28) for κ_r. The function $g(r)$ in the expression of κ_r has the following form:

$$g(r) = -\frac{(r - r_0)^2}{(\Delta r)^2}, \tag{37}$$

where r_0 and Δr are chosen to fit the radial profile of the mode. The latter is extracted from the GYSELA simulation with the same set of parameters as the linear code and for the corresponding mode. Even though κ_r allows the code to take into account global effects to some extent, it remains a local code by essence since we choose a radius r_p for which the dispersion relation is solved. Note that the closer to zero the value of ρ^* is, the more accurate the local approximation will be.[36] The plasma quantities are evaluated at the location $r_p \approx r_{0,max}$, which corresponds to the position of the peak for the maximal radial amplitude $\phi(r)$ among the m modes, for a given n.

A. Case with the ITG instability only

We take $\eta = \kappa_T/\kappa_n = 4$ and $\left|M_\parallel \frac{\kappa_{v_\parallel}}{\kappa_n}\right| = 0$, following the parameters chosen in Ref. 6, during the whole simulation, so only the ITG instability criterion is satisfied. Here, we have defined $M_\parallel = v_{\parallel,i}/c_s$ the parallel Mach number and $\kappa_{v_\parallel} = \partial_r \ln(v_{\parallel,i})$. In Fig. 9(a), we compare the growth rates determined by the GYSELA code to the growth rates

TABLE I. Summary of the results presented in Figs. 3–8 regarding the coexistence of ITG and PVG in the linear regime. The range of the normalized parameters, the dominant instability, and key observations for each case are listed.

	Parameters range				
Fig. #	κ_T, κ_n	$\frac{dv_\parallel}{dr}$	m, n	Main instability	Key observations
3	$\kappa_T \in [-1000, 1000]$	0	$m \in [0, 500]$ $n \in [-75, 0]$	ITG (for $\eta > 2$)	PVG not triggered ITG threshold visible at $\eta \approx 2$
	$\kappa_n = 200$	-0.01		PVG for $0 \leq \eta \leq 2$ ITG dominant for $\eta > 2$	Stabilizing effect of κ_T on PVG Destabilizing effect of $dv_\parallel/dr$ on ITG
		-0.03		PVG	Strong PVG drive $\gamma > 0$ for any value of η
4		$0, -0.01, -0.03$	$m = 80$ $n = -20$	Same as Fig. 3	Asymmetry in $\gamma(\eta)$ Unstable regions in Figs. 5 and 6
5	$\kappa_T \in [-1000, 1000]$ $\kappa_n \in [-250, 250]$	0		ITG	Unstable regions asymmetric in κ_T Kinetic and fluid thresholds can have opposite asymmetries
6		-0.01		...	For small κ_n, $\gamma > 0$ for any value of η
7	$\kappa_T \in [-1000, 1000]$ $\kappa_n = 200$	$0, -0.01, -0.03$	$m \in [0, 500]$ $n \in [-75, 0]$	...	No jump from an instability branch to another
8	$\kappa_T = 0, 200$ $\kappa_n = 200$	$\in [-0.025, 0]$		PVG	Stabilizing effect of κ_T on PVG
	$\kappa_T = 600$ $\kappa_n = 200$			ITG for 0.0125 PVG for $dv_\parallel/dr < -0.0125$	

TABLE II. Normalized parameters chosen for the GYSELA simulations. Δt denotes the time step. N_r, N_θ, N_φ, $N_{v_\parallel}$, N_μ are respectively the number of grid points along the r, θ, φ, $v_\parallel$, and μ directions. $\rho^* = \rho_{c,i}/a$ is the normalized gyroradius, $1/\epsilon = R_0/a$ is the aspect ratio, and q is the safety factor. The maximum density and temperature gradients for the deuterium are located at $r/a = 0.5$. The radial profile of the heat source is defined by $\rho_{s,heat} = 0.01$ and $L_{s,heat} = 0.1$ and the radial profile of the momentum source by $\rho_{s,mom} = 0.44$ and $L_{s,mom} = 0.015$ [see Eqs. (4) and (5)]. The momentum source is activated in the "PVG only" and "ITG and PVG" simulations at the time t_1. In the "PVG only" case, we activate the momentum source from the beginning of the simulation. We first choose a high value of amplitude, then a small value once the PVG criterion is satisfied at approximately $t_2 = 9000\Omega_{c0}^{-1}$. In the "ITG and PVG" case, we wait until $t_1 = 74000\Omega_{c0}^{-1}$ before activating the momentum source to allow the ITG modes to grow sufficiently. Then, we choose a high value of $S_0^{v_\parallel}$, so the PVG instability threshold is quickly exceeded. Once this criterion is satisfied, the amplitude of the momentum source is set to zero at $t_2 = 80000\Omega_{c0}^{-1}$ and for the rest of the simulation.

Parameters	ITG only	PVG only	ITG and PVG
Z_i, A_i		1, 2	
$\Delta t[\Omega_{c0}^{-1}]$		20	
$N_r \times N_\theta \times N_\varphi \times N_{v_\parallel} \times N_\mu$		$256 \times 257 \times 65 \times 128 \times 1$	
ρ^*		$1/200$	
$1/\epsilon$		100	
q		10^{30}	
τ		1	
$\kappa_n[-R_0^{-1}](r/a = 0.5)$		20	
$\kappa_T[-R_0^{-1}](r/a = 0.5)$	80	20	80
S_0^E		0.0003	
$S_0^{v_\parallel}$ (between t_1 and t_2)	0	0.01	0.02
$S_0^{v_\parallel}$ (between t_2 and $t \to \infty$)	0	0.0005	0
$t_1[\Omega_{c0}^{-1}]$	–	0	74 000
$t_2[\Omega_{c0}^{-1}]$	–	9000	80 000
$\Delta r[\rho_0]$	21.7	4.0	

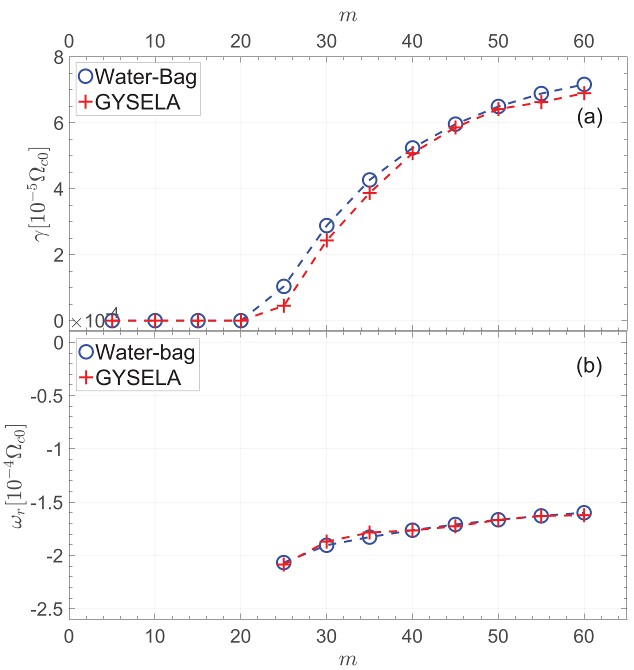

FIG. 9. (a) Instability growth rate γ plotted against the mode number m for the case "ITG only," with $n = -3$ and $\rho = 0.48$. (b) Angular frequency ω_r plotted against the mode number m for the case "ITG only," with $n = -3$ and $\rho = 0.5$. Note that ω_r is negative here because the perturbation wave associated with ITG propagates in the direction opposite to the electron diamagnetic velocity. The *m-axis* is shared between the two graphs.

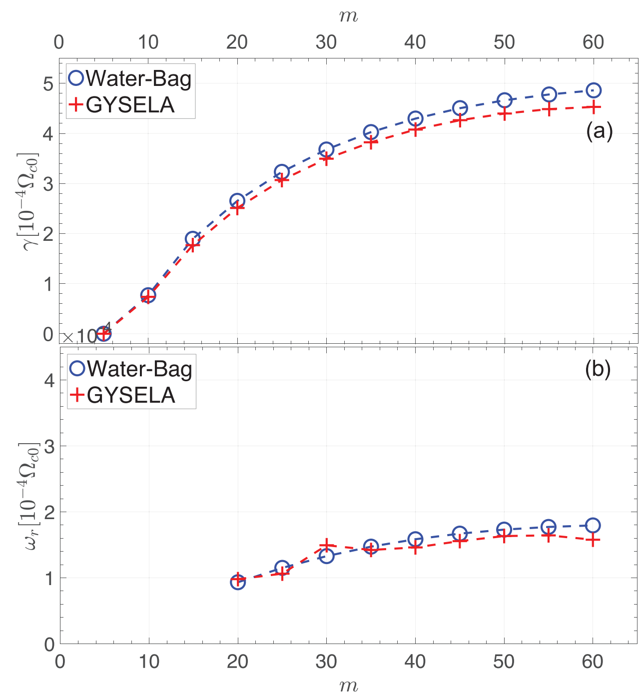

FIG. 10. (a) Instability growth rate γ plotted against the mode number m for the case "PVG only," with $n = -3$ and $\rho = 0.47$. (b) Angular frequency ω_r plotted against the mode number m for the case "PVG only," with $n = -3$ and $\rho = 0.5$. The frequencies are positive because the PVG instabilities propagate in the same direction as the electron diamagnetic velocity. The *m-axis* is shared between the two graphs.

obtained through the linear cylindrical code by plotting them against the azimuthal mode numbers m, for a given axial mode n. We see that for the values of n and ρ we chose, the modes $m \leq 20$ are linearly stable. The same procedure is applied to the angular frequencies and represented in Fig. 9(b). As expected, ω_r is negative because the perturbation wave associated with ITG propagates in the direction opposite to the electron diamagnetic drift, in our convention. Indeed, with the right-hand rule for $\mathbf{u}_\theta$ with respect to $\mathbf{B}$, the electron diamagnetic drift is in the same direction as $\mathbf{u}_\theta$. In both cases, we find a very good agreement between the two curves, despite the fact that we compare a global nonlinear code with a local linear one. Note that, unlike the growth rate, the dependence of ω_r on the choice of r_p is weak, as shown in Ref. 19. This could explain why the discrepancy between the GYSELA curve and the linear code curve is smaller for ω_r than for γ.

B. Case with the PVG instability only

We take $\eta = 1$ and $\left|M_\parallel \frac{\kappa_{v_\parallel}}{\kappa_n}\right| \approx 3$ (with $M_\parallel \approx 0.018$) at the time γ and ω_r are computed, so only the PVG instability is triggered. The comparison between the GYSELA code and the linear code in terms of growth rate is plotted in Fig. 10(a), while the comparison in terms of angular frequency is plotted in Fig. 10(b). Once again, a very good agreement is found between the two codes. The perturbation modes associated with the PVG instability are unstable for lower values of m compared to the case presented in Sec. IV A, at least for the values of n and ρ used. Also, the growth rates of PVG are approximately one order higher than the growth rates of ITG for the chosen parameters. In Fig. 10(b), the angular frequencies are positive because the PVG instability propagates in the electron diamagnetic velocity direction.

C. Case where the ITG and PVG instabilities coexist

We perform a simulation where we attempt to trigger both the ITG and PVG instabilities by taking $\eta = 4$ and $\left|M_\parallel \frac{\kappa_{v_\parallel}}{\kappa_n}\right| \approx 3.57$. The growth rates and angular frequencies obtained with the GYSELA code and Water-bag code in this case can be found in Fig. 11. We see that a good agreement is also obtained between the curves in a situation where ITG and PVG instabilities coexist. The positive angular frequencies in Fig. 11(b) seem to indicate that the modes are dominated by the PVG instability. Both the PVG and ITG instability criteria are satisfied. In this setup, we can expect two possibilities: 1. the coexistence of PVG branch and ITG branch or 2. a single PVG-ITG hybrid branch, that is, a series of modes influenced by both ion temperature and parallel velocity gradients. The Water-bag code shows that there is only a single unstable linear solution for each mode plotted in Fig. 11. Therefore, we are in the second situation: PVG-ITG hybrid instability.

It should also be mentionned that in Figs. 9–11, the criterion $k_\theta k_\parallel dv_\parallel/dr > 0$[11,34] is satisfied since the axial mode number n and the parallel velocity gradient $dv_\parallel/dr$ are negatives in all three simulations. Modes with $m > 0$ are indeed unstable in these simulations.

With these results and the ones presented in Secs. IV A and IV B, we can conclude that GYSELA is a reliable tool to perform linear analysis in cylindrical geometry, as long as the parameters of Sec. II B are

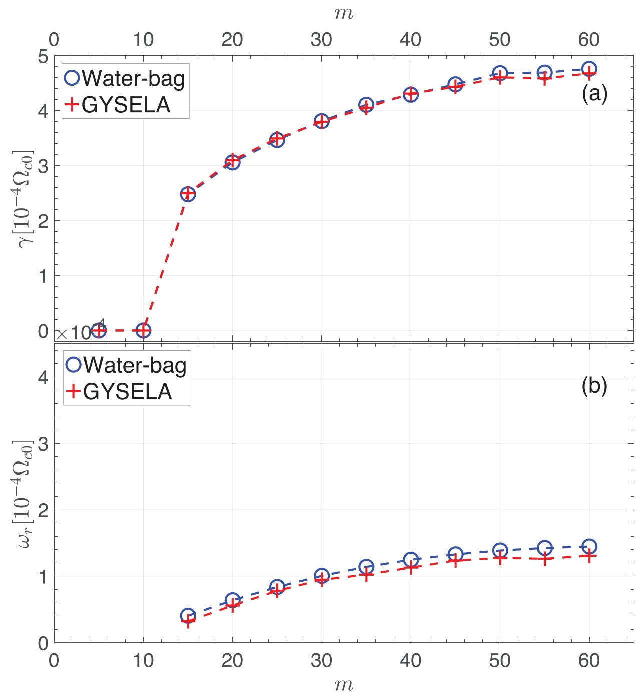

FIG. 11. (a) Instability growth rate γ and (b) angular frequency ω_r, plotted against the mode number m for the case "ITG+PVG," with $n = -2$ and $\rho = 0.47$. The positive angular frequencies indicate modes dominated by the PVG instability. The *m-axis* is shared between the two graphs.

used. The next step will be to operate this "cylindrical version" of GYSELA in the nonlinear regime to study if it can accurately predict the transport of particles, which will require to alleviate the adiabatic response assumption for the electrons, heat, and momentum observed in experimental cylindrical devices.

V. CONCLUSION

In summary, we have investigated the linear interplay between ITG and PVG instabilities in cylindrical geometry, using two complementary approaches: a Water-bag kinetic model and the 5D full-f gyrokinetic code GYSELA.

By discretizing the ion velocity distribution into a set of bags and retaining finite parallel flows, the Water-bag approach yields an analytical dispersion relation (in the form of a high-order polynomial in the complex frequency) that incorporates both ITG and PVG drive terms (radial gradients of temperature and parallel velocity), as well as finite-Larmor-radius effects. Moreover, the radial dependence of equilibrium profiles was introduced via a semi-global *ansatz*.

We confirmed these theoretical predictions by comparing them against global gyrokinetic simulations carried out with a modified version of GYSELA that effectively mimics cylindrical conditions. We emulate a cylindrical configuration by removing toroidal curvature and setting a high safety factor. Using heat and momentum sources, the code was able to excite ITG and PVG modes in a controlled manner. Despite the global nature of the gyrokinetic simulations and the semi-global nature of our Water-bag approach, we achieved quantitative agreement in both growth rate and mode frequency for various values of radial gradients of temperature and parallel velocity, over a wide range of azimuthal and axial mode numbers.

We applied the Water-bag analytical dispersion relation to identify key parametric dependencies of ITG and PVG modes. We showed that the ITG is strongly enhanced by parallel flow shear. The PVG is stabilized by the ion temperature gradient if it is relatively weak, but larger ion temperature gradients lead to an overall enhancement of the instability.

In addition, we described the instability threshold obtained from both our Water-bag model and a fluid model, which highlights kinetic effects by comparison. The kinetic modification of the instability threshold is significant, especially when the density gradient and temperature gradient have opposite directions.

These results confirm the applicability of gyrokinetic methods to cylindrical devices and highlight the importance of parallel flow shear in shaping microinstabilities. Future work will focus on nonlinear coupling mechanisms (based on nonlinear gyrokinetic simulations) and the resulting transport properties. Future studies will incorporate kinetic electron effects and collisional damping, enabling the exploration of turbulence saturation and transport in regimes closer to real laboratory conditions. Collisions among charged particles, as well as between charged particles and neutrals, are essential in low-temperature plasmas and will need to be taken into consideration for a more realistic modeling. Similarly, the physics of plasma–wall interaction will need to be taken into account as it affects the electric potential response along the magnetic field lines.[37] The recent developments performed in the GYSELA code should allow one to address these important issues in the near future.[38] Meanwhile, improved experimental diagnostics in linear devices such as SPEKTRE will help benchmark these simulation predictions with measured fluctuations and transport profiles.

ACKNOWLEDGMENTS

This work has been carried out within the framework of the EUROfusion Consortium, funded by the European Union via the Euratom Research and Training Programme (Grant Agreement No. 101052200-EUROfusion). Views and opinions expressed are, however, those of the author(s) only and do not necessarily reflect those of the European Union or the European Commission. Neither the European Union nor the European Commission can be held responsible for them. This project was provided with computing HPC and storage resources by GENCI at TGCC thanks to the grant 2024-A0160502224 on the supercomputer Joliot Curie's SKL/ROME partition.

AUTHOR DECLARATIONS

Conflict of Interest

The authors have no conflicts to disclose.

Author Contributions

T. Rouyer: Data curation (lead); Formal analysis (lead); Investigation (lead); Methodology (lead); Validation (lead); Visualization (lead); Writing – original draft (equal); Writing – review & editing (equal). **M. Lesur:** Conceptualization (equal); Formal analysis (supporting); Funding acquisition (equal); Investigation (supporting); Methodology (supporting); Project administration (equal); Resources (equal);

Supervision (equal); Writing – original draft (equal); Writing – review & editing (equal). **E. Gravier:** Conceptualization (equal); Formal analysis (supporting); Funding acquisition (equal); Investigation (supporting); Methodology (equal); Project administration (equal); Resources (equal); Supervision (equal); Writing – original draft (equal); Writing – review & editing (equal). **X. Garbet:** Conceptualization (supporting); Funding acquisition (equal); Investigation (supporting); Methodology (equal); Supervision (supporting); Writing – review & editing (equal). **Y. Sarazin:** Conceptualization (supporting); Funding acquisition (equal); Investigation (supporting); Methodology (equal); Supervision (supporting); Writing – review & editing (equal). **K. Lim:** Investigation (supporting); Methodology (supporting); Writing – review & editing (supporting). **G. Lo-Cascio:** Investigation (supporting); Methodology (supporting); Writing – review & editing (supporting).

DATA AVAILABILITY

The data that support the findings of this study are available from the corresponding author upon reasonable request.

REFERENCES

[1]G. S. Lee and P. H. Diamond, "Theory of ion-temperature-gradient-driven turbulence in tokamaks," Phys. Fluids **29**, 3291 (1986).
[2]S. C. Cowley, R. M. Kulsrud, and R. Sudan, "Considerations of ion-temperature-gradient-driven turbulence," Phys. Fluids B **3**, 2767 (1991).
[3]A. J. Brizard and T. S. Hahm, "Foundations of nonlinear gyrokinetic theory," Rev. Mod. Phys. **79**, 421 (2007).
[4]J. W. Connor and H. R. Wilson, "Survey of theories of anomalous transport," Plasma Phys. Controlled Fusion **36**, 719 (1994).
[5]P. J. Catto, M. N. Rosenbluth, and C. S. Liu, "Parallel velocity shear instabilities in an inhomogeneous plasma with a sheared magnetic field," Phys. Fluids **16**, 1719 (1973).
[6]X. Garbet, C. Fenzi, H. Capes, P. Devynck, and G. Antar, "Kelvin-Helmholtz instabilities in tokamak edge plasmas," Phys. Plasmas **6**, 3955 (1999).
[7]Y. B. Kim, P. H. Diamond, and R. J. Groebner, "Neoclassical poloidal and toroidal rotation in tokamaks," Phys. Fluids **3**, 2050–2060 (1991).
[8]J. F. Drake, A. B. Hassam, P. N. Guzdar, C. S. Liu, and D. McCarthy, "Loss of static equilibrium, flow generation and the development of turbulence at the edge of tokamaks," Nucl. Fusion **32**, 1657 (1992).
[9]C. S. Chang and S. Ku, "Spontaneous rotation sources in a quiescent tokamak edge plasma," Phys. Plasmas **15**, 062510 (2008).
[10]F. I. Parra and M. Barnes, "Intrinsic rotation in tokamaks: Theory," Plasma Phys. Controlled Fusion **57**, 045002 (2015).
[11]Y. Kosuga, S.-I. Itoh, and K. Itoh, "Density peaking by parallel flow shear driven instability," Plasma Fusion Res. **10**, 3401024 (2015).
[12]Y. Kosuga, S.-I. Itoh, and K. Itoh, "Zonal flow generation in parallel flow shear driven turbulence," Phys. Plasmas **24**, 032304 (2017).
[13]Y. Kosuga, "How pattern is selected in drift wave turbulence: Role of parallel flow shear," Phys. Plasmas **24**, 122305 (2017).
[14]T. Kaneko, H. Tsunoyama, and R. Hatakeyama, "Drift-wave instability excited by field-aligned ion flow velocity shear in the absence of electron current," Phys. Rev. Lett. **90**, 125001 (2003).
[15]O. F. Castellanos, E. Anabitarte, J. M. Sentíes, C. Hidalgo, and M. A. Pedrosa, "Parallel flows and turbulence in a linear plasma machine," Plasma Phys. Controlled Fusion **47**, 2067 (2005).
[16]S. Inagaki, T. Kobayashi, Y. Kosuga, S.-I. Itoh, T. Mitsuzono, Y. Nagashima, H. Arakawa, T. Yamada, Y. Miwa, N. Kasuya *et al.*, "A concept of cross-ferroic plasma turbulence," Sci. Rep. **6**, 22189 (2016).
[17]T. Kobayashi, S. Inagaki, Y. Kosuga, M. Sasaki, Y. Nagashima, T. Yamada, H. Arakawa, N. Kasuya, A. Fujisawa, S.-I. Itoh *et al.*, "Structure formation in parallel ion flow and density profiles by cross-ferroic turbulent transport in linear magnetized plasma," Phys. Plasmas **23**, 102311 (2016).
[18]F. Brochard, D. Geneve, S. Heuraux, V. Bobkov, D. Del Sarto, E. Faudot, A. Ghizzo, E. Gravier, N. Lemoine, M. Lesur *et al.*, "SPEKTRE, a linear radiofrequency device for investigating edge plasma physics," in 49th EPS Conference on Plasma Physics, Bordeaux, France, July 2023. https://hal.science/hal-04171543.
[19]E. Gravier, F. Brochard, M. Lesur, J. Moritz, S. Heuraux, D. Geneve, T. Rouyer, D. Del Sarto, E. Faudot, A. Ghizzo *et al.*, "Drift waves and ion temperature gradient instabilities in the large linear device SPEKTRE," Phys. Plasmas **31**, 112104 (2024).
[20]J. Bourgeois, M. Lesur, G. Cuerva-Lazaro, and Y. Kosuga, "Impurity parallel velocity gradient instability," Open Plasma Sci. **1**, 1 (2024).
[21]S. L. Newton, S. C. Cowley, and N. F. Loureiro, "Understanding the effect of sheared flow on microinstabilities," Plasma Phys. Controlled Fusion **52**, 125001 (2010).
[22]M. Barnes, F. I. Parra, E. G. Highcock, A. A. Schekochihin, S. C. Cowley, and C. M. Roach, "Turbulent transport in tokamak plasmas with rotational shear," Phys. Rev. Lett. **106**, 175004 (2011).
[23]E. G. Highcock, M. Barnes, F. I. Parra, A. A. Schekochihin, C. M. Roach, and S. C. Cowley, "Transport bifurcation induced by sheared toroidal flow in tokamak plasmas," Phys. Plasmas **18**, 102304 (2011).
[24]A. A. Schekochihin, E. G. Highcock, and S. C. Cowley, "Subcritical fluctuations and suppression of turbulence in differentially rotating gyrokinetic plasmas," Plasma Phys. Controlled Fusion **54**, 055011 (2012).
[25]P. Morel, E. Gravier, N. Besse, R. Klein, A. Ghizzo, P. Bertrand, X. Garbet, P. Ghendrih, V. Grandgirard, and Y. Sarazin, "Gyrokinetic modeling: A multi-water-bag approach," Phys. Plasmas **14**, 112109 (2007).
[26]V. Grandgirard, J. Abiteboul, J. Bigot, T. Cartier-Michaud, N. Crouseilles, G. Dif-Pradalier, C. Ehrlacher, D. Esteve, X. Garbet, P. Ghendrih *et al.*, "A 5D gyrokinetic full-f global semi-Lagrangian code for flux-driven ion turbulence simulations," Comput. Phys. Commun. **207**, 35 (2016).
[27]D. Esteve, Y. Sarazin, X. Garbet, V. Grandgirard, S. Breton, P. Donnel, Y. Asahi, C. Bourdelle, G. Dif-Pradalier, C. Ehrlacher *et al.*, "Self-consistent gyrokinetic modeling of neoclassical and turbulent impurity transport," Nucl. Fusion **58**, 036013 (2018).
[28]Y. Sarazin, V. Grandgirard, J. Abiteboul, S. Allfrey, X. Garbet, P. Ghendrih, G. Latu, A. Strugarek, G. Dif-Pradalier, P. H. Diamond *et al.*, "Predictions on heat transport and plasma rotation from global gyrokinetic simulations," Nucl. Fusion **51**, 103023 (2011).
[29]J. S. deGrassie, R. J. Groebner, and K. H. Burrell, "Prompt toroidal momentum balance with collisionless neutral beam injected torque in DIII-D," Phys. Plasmas **13**, 112507 (2006).
[30]E. Gravier and E. Plaut, "Kinetic water-bag model of global collisional drift waves and ion temperature gradient instabilities in cylindrical geometry," Phys. Plasmas **20**, 042105 (2013).
[31]R. Klein, E. Gravier, P. Morel, N. Besse, and P. Bertrand, "Gyrokinetic water-bag modeling of a plasma column: Magnetic moment distribution and finite Larmor radius effects," Phys. Plasmas **16**, 082106 (2009).
[32]R. F. Ellis, E. Marden-Marshall, and R. Majeski, "Collisional drift instability of a weakly ionized argon plasma," Plasma Phys. **22**, 113 (1980).
[33]E. Gravier, E. Plaut, X. Caron, and M. Jenny, "Transitions between drift waves in a magnetized cylindrical plasma: Experiments and fluid model, solved with a spectral method," Eur. Phys. J. D **67**, 7 (2013).
[34]N. D'Angelo, "Kelvin—Helmholtz instability in a fully ionized plasma in a magnetic field," Phys. Fluids **8**, 1748–1750 (1965).
[35]S. Mazzi, Y. Camenen, J. Garcia, D. Zarzoso, D. Frigione, L. Garzotti, F. Rimini, D. Van Eester, and JET Contributors. "Effects of the parallel flow shear on the ITG-driven turbulent transport in tokamak plasmas," Nucl. Fusion **62**, 096024 (2022).
[36]J. Candy, R. E. Waltz, and W. Dorland, "The local limit of global gyrokinetic simulations," Phys. Plasmas **11**, L25–L28 (2004).
[37]P. C. Stangeby, *The Plasma Boundary of Magnetic Fusion Devices* (Institute of Physics Publishing, Bristol, 2000).
[38]Y. Munschy, "Kinetic and gyrokinetic physics of plasma-wall interaction in tokamaks," Ph.D. thesis (Aix-Marseille University, 2024).